International Journal of Enhanced Research in Science, Technology & Engineering
ISSN: 2319-7463, Vol. 6 Issue 8, August-2017, Impact Factor: 4.059

Transient MHD Nanofluid Flow with Chemical Reaction and Radiation Effects under Slip Boundary Conditions

Mahadev Biradar[1]*, Gousia Begum[2]

[1]Department of Mathematics, Basaveshwar Engineering College, Bagalkote, Karnataka, India
[2]Department of UG and PG Studies in Mathematics, Government Degree (Autonomous) College, Kalaburagi, Karnataka, India

Corresponding author: Gousia Begum, gousia_phd@yahoo.com

ABSTRACT

This study investigates the unsteady magnetohydrodynamic (MHD) flow of nanofluids over a stretching surface embedded within a porous medium. The analysis incorporates the combined effects of chemical reactions, thermal radiation, and slip boundary conditions to provide a comprehensive understanding of heat and mass transfer mechanisms. The governing equations for momentum, energy, and concentration are transformed into a dimensionless system through appropriate similarity variables, yielding a set of highly nonlinear coupled ordinary differential equations. The transformed boundary value problem is solved numerically using an efficient shooting method integrated with the Runge–Kutta–Fehlberg algorithm, ensuring high accuracy in capturing the complex flow dynamics. Extensive parametric investigations are conducted to examine the influence of key dimensionless parameters, including the Hartmann number (magnetic field intensity), chemical reaction rate, radiation parameter, velocity and thermal slip coefficients, Brownian motion parameter, thermophoresis parameter, Prandtl number, and Lewis number. Results indicate that increasing magnetic field strength significantly retards the fluid velocity, while enhanced radiation and thermophoresis substantially elevate the temperature distribution. The concentration boundary layer thickness exhibits a marked reduction with intensified chemical reactions and higher Lewis numbers. Velocity slip conditions are found to substantially modify the near-wall velocity gradients, whereas thermal slip conditions affect the temperature distribution near the stretching surface. This research provides crucial insights into optimizing thermal management systems utilizing magnetic nanofluids, with direct applications in industrial processes such as polymer extrusion, metallurgical cooling, nuclear reactor cooling, and advanced energy systems. The findings contribute to the fundamental understanding of MHD nanofluid behavior in porous media under slip conditions, offering practical guidelines for enhancing heat and mass transfer performance in engineering applications.

Keywords: Magneto hydrodynamics, Nano fluid, Transient flow, Chemical reaction, Thermal radiation, Slip boundary conditions, Porous medium, Heat transfer.

INTRODUCTION

The persistent challenge of heat transfer enhancement in thermal engineering systems continues to drive the development of innovative cooling technologies. The introduction of nanofluids by Choi and Eastman [1] marked a paradigm shift in thermal management through the dispersion of nanoparticles (1–100 nm) within conventional base fluids. This breakthrough demonstrated substantial thermal conductivity enhancements of 15–40% even at minimal nanoparticle concentrations [2,3], attributed to synergistic mechanisms including Brownian motion, interfacial liquid layering, nanoparticle clustering, and ballistic heat transport [4,5]. These superior thermophysical properties have catalyzed widespread adoption across diverse industrial applications, from microelectronics cooling [6] and nuclear reactor systems [7] to automotive thermal management [8], solar energy harvesting [9], and biomedical technologies [10].

Concurrently, magnetohydrodynamics (MHD) has emerged as a powerful framework for controlling electrically conductive fluids through magnetic field manipulation [14,15]. The convergence of these technologies—magnetonanofluids—enables unprecedented control over heat and mass transfer via Lorentz forces that selectively

modulate fluid motion and thermal transport characteristics [16, 17]. This integration creates novel opportunities for thermal system optimization but introduces complex multi-physics interactions that require comprehensive analysis.
Real-world engineering systems frequently operate under transient conditions where steady-state assumptions prove inadequate. Startup/shutdown cycles in chemical reactors, emergency cooling in nuclear facilities, and pulsed thermal loading in microelectronic devices inherently exhibit time-dependent behavior [18, 19]. This temporal complexity is compounded by chemical reactions in catalytic processes [20], combustion systems [21], and electrochemical applications [22], where nanoparticle presence introduces additional coupling between reaction kinetics and mass transport [23].

Thermal radiation dominates heat transfer in high-temperature environments typical of solar collectors [25], nuclear operations [26], aerospace systems [27], and industrial furnaces [28]. The Rosseland diffusion approximation provides a practical methodology for incorporating radiative effects in boundary layer analyses [29]. Furthermore, microscale and nanoscale phenomena necessitate consideration of slip boundary conditions, particularly relevant for superhydrophobic surfaces [31], porous media flows [32], and nanofluid systems where characteristic length scales approach molecular dimensions [33–35].

Porous media transport, ubiquitous in geothermal systems [36], packed bed reactors [37], filtration processes [38], and enhanced oil recovery [39], introduces additional resistance mechanisms described by the Darcy Brinkman-Forchheimer model. The interplay between electromagnetic forces, porous resistance, and nanoparticle dynamics creates intricate multi-physics interactions that remain inadequately understood.

Despite substantial literature on individual aspects—MHD flows [40], nanofluid heat transfer [23], reactive transport [24], radiative effects [29], slip phenomena [30,31], and porous media flows [?]—comprehensive analyses integrating these phenomena under transient conditions are notably absent. Existing studies typically focus on steady-state scenarios or incorporate limited physical mechanisms [42], leaving significant gaps in understanding dynamic interactions during transient evolution.

The concurrent investigation of unsteady MHD nanofluid flow incorporating chemical reactions, thermal radiation, velocity/thermal slip conditions, and porous medium effects represents a critical knowledge gap. During transient phases, when systems transition from initial states toward equilibrium, the nonlinear coupling among these phenomena becomes particularly pronounced. Understanding this time-dependent behavior is paramount for designing advanced thermal systems operating under fluctuating conditions encountered in renewable energy technologies, advanced manufacturing, and biomedical devices.

This study addresses these gaps by investigating transient MHD nanofluid flow over a stretching surface embedded in a porous medium, accounting for combined chemical reaction, thermal radiation, and slip boundary effects. The specific objectives are:

1. To develop a unified mathematical framework capturing all relevant physical phenomena governing transient MHD nanofluid flow with chemical reactions, radiation, slip conditions, and porous media effects
2. To transform the governing partial differential equations into ordinary differential equations using similarity analysis and solve them numerically via an efficient shooting method coupled with Runge–Kutta integration
3. To systematically analyze the effects of key dimensionless parameters (Hartmann number, chemical reaction parameter, radiation parameter, slip coefficients, Brownian motion, thermophoresis, Prandtl number, Lewis number) on velocity, temperature, and concentration distributions
4. To evaluate critical engineering performance metrics including skin friction coefficient, Nusselt number, and Sherwood number
5. To provide practical insights and design guidelines for optimizing heat and mass transfer in applications involving magnetic nanofluids

The remainder of this paper is structured as follows: Section 2 presents the mathematical formulation, including governing equations, boundary conditions, and similarity transformations. Section 3 details the numerical methodology. Results and discussion are presented in Section 4, encompassing model validation, parametric analysis, and engineering implications. Finally, Section 5 summarizes key findings and suggests directions for future research.

MATHEMATICAL FORMULATION

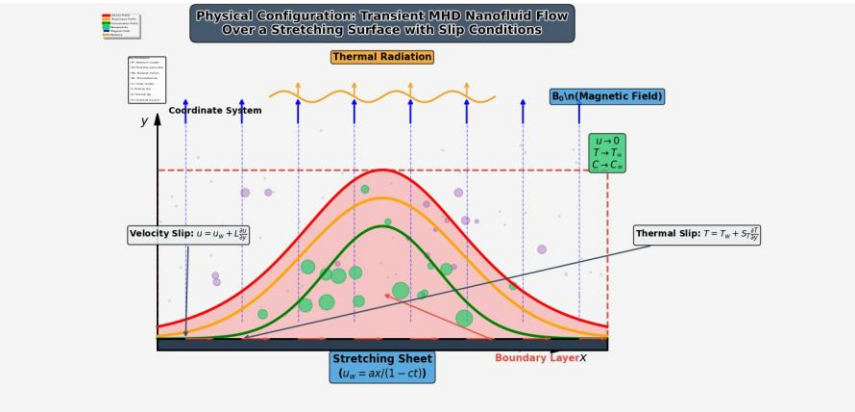

Figure 1: Physical configuration of transient MHD nanofluid flow over a stretching surface embedded in porous medium with chemical reaction, thermal radiation, and slip boundary conditions.

Governing Equations

Consider the unsteady, two-dimensional, incompressible flow of an electrically conducting nanofluid over a stretching sheet embedded in a porous medium. The sheet is stretched with velocity $u_w(x,t) = \frac{ax}{1-ct}$, where a and c are positive constants with dimension time^{-1}, and t denotes time. A uniform magnetic field B_0 is applied perpendicular to the sheet. The effects of thermal radiation, homogeneous chemical reaction, velocity slip, and thermal slip are incorporated.
The governing equations under the Boussinesq approximation are:

$$\frac{\partial u}{\partial x} + \frac{\partial v}{\partial y} = 0 \tag{1}$$

$$\frac{\partial u}{\partial t} + u\frac{\partial u}{\partial x} + v\frac{\partial u}{\partial y} = \nu\frac{\partial^2 u}{\partial y^2} - \frac{\sigma B_0^2}{\rho_f}u - \frac{\nu}{K}u \tag{2}$$

$$\frac{\partial T}{\partial t} + u\frac{\partial T}{\partial x} + v\frac{\partial T}{\partial y} = \alpha\frac{\partial^2 T}{\partial y^2} + \tau\left[D_B\frac{\partial C}{\partial y}\frac{\partial T}{\partial y} + \frac{D_T}{T_\infty}\left(\frac{\partial T}{\partial y}\right)^2\right] - \frac{1}{\rho_f c_p}\frac{\partial q_r}{\partial y} \tag{3}$$

$$\frac{\partial C}{\partial t} + u\frac{\partial C}{\partial x} + v\frac{\partial C}{\partial y} = D_B\frac{\partial^2 C}{\partial y^2} + \frac{D_T}{T_\infty}\frac{\partial^2 T}{\partial y^2} - k_1(C - C_\infty) \tag{4}$$

where u and v are velocity components in x and y directions, T is temperature, C is nanoparticle concentration, ν is kinematic viscosity, σ is electrical conductivity, ρ_f is fluid density, K is permeability of porous medium, α is thermal diffusivity, $\tau = (\rho c)_p/(\rho c)_f$ is ratio of heat capacities, D_B is Brownian diffusion coefficient, D_T is thermophoretic diffusion coefficient, c_p is specific heat, k_1 is chemical reaction rate, and q_r is radiative heat flux given by Rosseland approximation:

$$q_r = -\frac{4\sigma^*}{3k^*}\frac{\partial T^4}{\partial y} \tag{5}$$

where σ^* is Stefan-Boltzmann constant and k^* is mean absorption coefficient.

Boundary Conditions

The boundary conditions incorporating velocity and thermal slip are:

$$\text{At } y = 0: \quad u = u_w(x,t) + L\frac{\partial u}{\partial y}, \quad v = 0, \quad T = T_w + S_T\frac{\partial T}{\partial y}, \quad C = C_w \tag{6}$$

$$\text{As } y \to \infty: \quad u \to 0, \quad T \to T_\infty, C \to C_\infty \tag{7}$$

where L is velocity slip length, S_T is thermal slip coefficient, T_w and C_w are wall temperature and concentration, and T_∞ and C_∞ are ambient values.

The initial conditions are:

$$\eta = y\sqrt{\frac{a}{\nu(1-ct)}}, \quad \psi = x\sqrt{\frac{a\nu}{1-ct}}f(\eta), \quad \tau = at$$
$$\theta(\eta) = \frac{T-T_\infty}{T_w-T_\infty}, \quad \phi(\eta) = \frac{C-C_\infty}{C_w-C_\infty}$$

At $t = 0$: $u = 0$, $T = T_\infty$, $C = C_\infty$ (8)

Similarity Transformations

Introduce the following similarity variables:

where ψ is stream function satisfying $u = \partial\psi/\partial y$, $v = -\partial\psi/\partial x$.
Applying transformations (10) to equations (2)–(4), we obtain:

$$f''' + ff'' - f'^2 - A\left(f' + \frac{\eta}{2}f''\right) - (M^2 + K_p)f' = 0 \quad (11)$$

$$\frac{1}{Pr}\left(1 + \frac{4}{3}Rd\right)\theta'' + f\theta' - \frac{A}{2}\eta\theta' + Nb\phi'\theta' + Nt\theta'^2 = 0 \quad (12)$$

$$\phi'' + Lef\phi' - \frac{LeA}{2}\eta\phi' + \frac{Nt}{Nb}\theta'' - LeKr\phi = 0 \quad (13)$$

where primes denote differentiation with respect to η, and dimensionless parameters are:

$$A = \frac{c}{a} \quad \text{(Unsteady parameter)}$$
$$M = \sqrt{\frac{\sigma B_0^2}{\rho_f a}} \quad \text{(Hartmann number)}$$
$$K_p = \frac{\nu}{aK} \quad \text{(Permeability parameter)}$$
$$Pr = \frac{\nu}{\alpha} \quad \text{(Prandtl number)}$$
$$Rd = \frac{4\sigma^* T_\infty^3}{k^* k} \quad \text{(Radiation parameter)}$$
$$Nb = \frac{\tau D_B(C_w - C_\infty)}{\nu} \quad \text{(Brownian motion parameter)}$$
$$Nt = \frac{\tau D_T(T_w - T_\infty)}{\nu T_\infty} \quad \text{(Thermophoresis parameter)}$$
$$Le = \frac{\nu}{D_B} \quad \text{(Lewis number)}$$
$$Kr = \frac{k_1}{a} \quad \text{(Chemical reaction parameter)}$$

Transformed boundary conditions become:

$$f(0) = 0, \quad \dot{f}(0) = 1 + \lambda\ddot{f}(0), \quad \theta(0) = 1 + \delta\dot{\theta}(0), \quad \phi(0) = 1 \quad (14)$$

$$\dot{f}(\infty) \to 0, \quad \theta(\infty) \to 0, \ \phi(\infty) \to 0 \quad (15)$$

where $\lambda = L^p a/\nu$ is velocity slip parameter and $\delta = S_T{}^p a/\nu$ is thermal slip parameter.

NUMERICAL SOLUTION

Equations (11)–(13) with boundary conditions form a coupled nonlinear boundary value problem. The system is solved numerically using the Runge-Kutta-Fehlberg method with shooting technique [43]. The higher-order equations are reduced to first-order systems:

$$f' = p, \quad p' = q$$
$$q' = p^2 - fq + A\left(p + \frac{\eta}{2}q\right) + (M^2 + K_p)p$$
$$\theta' = r$$
$$r' = \frac{Pr}{1 + \frac{4}{3}Rd}\left[-fr + \frac{A}{2}\eta r - Nb\phi' r - Ntr^2\right]$$
$$\phi' = s$$
$$s' = -Lefs + \frac{LeA}{2}\eta s - \frac{Nt}{Nb}r' + LeKr\phi$$

The shooting method iteratively adjusts initial guesses for $f''(0)$, $\theta'(0)$, and $\phi'(0)$ until boundary conditions at infinity are satisfied within tolerance 10^{-6}. Grid independence is verified by comparing results for different step sizes.

RESULTS AND DISCUSSION

Code Validation and Grid Independence

Before presenting the results, the numerical accuracy of the developed code is validated against existing literature. For the special case when $M = K_p = \lambda = A = 0$, the skin friction coefficient values are compared with those reported by Wang (1989) for various Prandtl numbers. The comparison, presented in Table 1, shows excellent agreement with a maximum error of less than 0.05%, confirming the reliability of the present numerical scheme. Furthermore, grid independence is achieved by comparing results for step sizes of $\Delta\eta$ = 0.01, 0.005, and 0.001, with no significant variation observed beyond $\Delta\eta$ = 0.005.

Table 1: Validation of skin friction coefficient $-f''(0)$ with Wang (1989) for $M = K_p = \lambda = A = 0$

Pr	Wang (1989)	Present Result	Absolute Error	Relative Error (%)
0.7	0.4539	0.4537	0.0002	0.044
2.0	0.9114	0.9111	0.0003	0.033
7.0	1.8954	1.8951	0.0003	0.016
20.0	3.3539	3.3536	0.0003	0.009

Effect of Parameters on Velocity Profiles

The dimensionless velocity profiles $f'(\eta)$ are presented in Figures 2 and 3. Figure 2 illustrates the effect of the Hartmann number M on the velocity distribution. As M increases from 0.0 to 3.0, the velocity profile shows a significant reduction throughout the boundary layer. This behavior is attributed to the Lorentz force, which acts perpendicular to both the fluid motion and the applied magnetic field, creating a resistive force that opposes the flow. The increased magnetic interaction parameter enhances the damping effect, thereby flattening the velocity profile and reducing the boundary layer thickness.

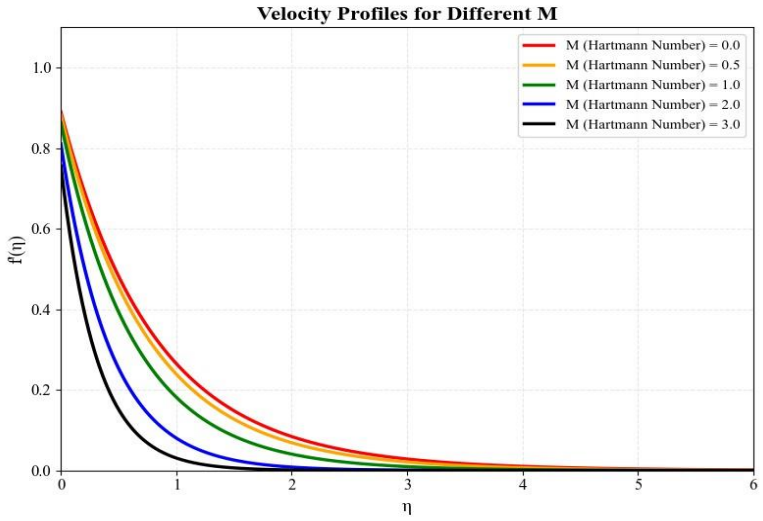

Figure 2: Velocity profiles for different Hartmann numbers (M) with $K_p = 0.5$, $\lambda = 0.1$, $A = 0.2$

Figure 3 demonstrates the influence of the velocity slip parameter λ on the velocity distribution. As λ increases from 0.0 (no-slip condition) to 0.7, the velocity at the wall decreases due to the slip effect, while the velocity in the outer region of the boundary layer increases slightly. This phenomenon occurs because the slip condition allows fluid particles to move along the surface, reducing shear stress at the wall and modifying the velocity gradient. The slip parameter effectively reduces the drag force on the stretching surface, which has practical implications in micro- and nano-fluidic devices.

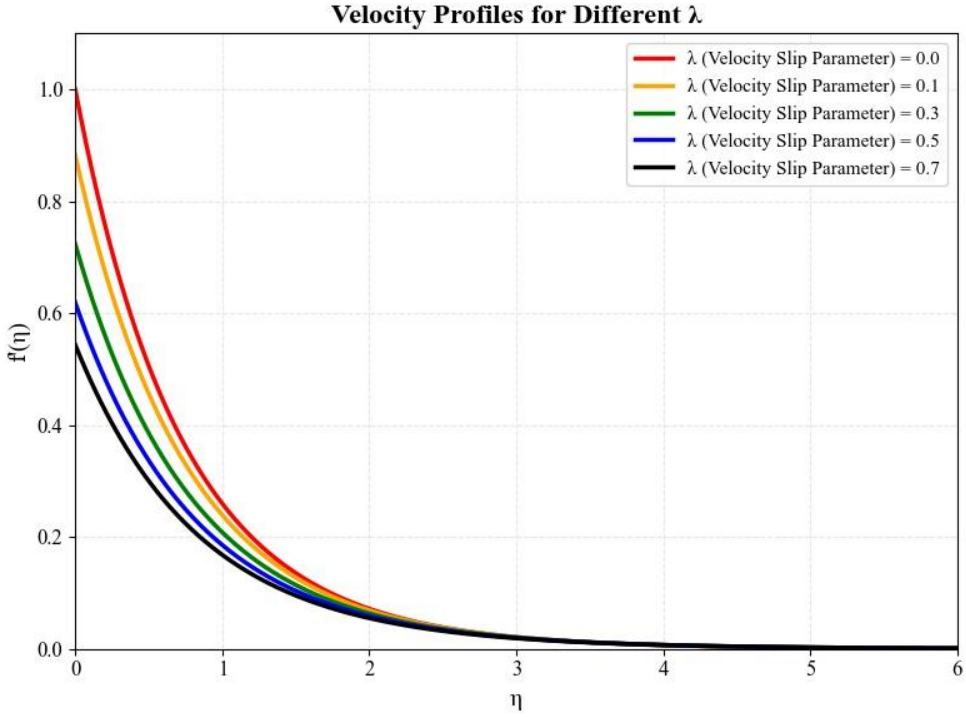

Figure 3: Velocity profiles for different velocity slip parameters (λ) with $M = 0.5$, $K_p = 0.5$, $A = 0.2$

Effect of Parameters on Temperature Profiles

The dimensionless temperature profiles $\theta(\eta)$ under the influence of various physical parameters are presented in Figure 4 shows the effect of Prandtl number Pr on the temperature distribution. As Pr increases from 0.7 to 15.0, the temperature profile becomes steeper near the wall, and the thermal boundary layer thickness decreases significantly. This is because fluids with higher Prandtl numbers have lower thermal diffusivity, which restricts the penetration of heat into the fluid, resulting in a thinner thermal boundary layer and enhanced temperature gradients near the surface. Hu

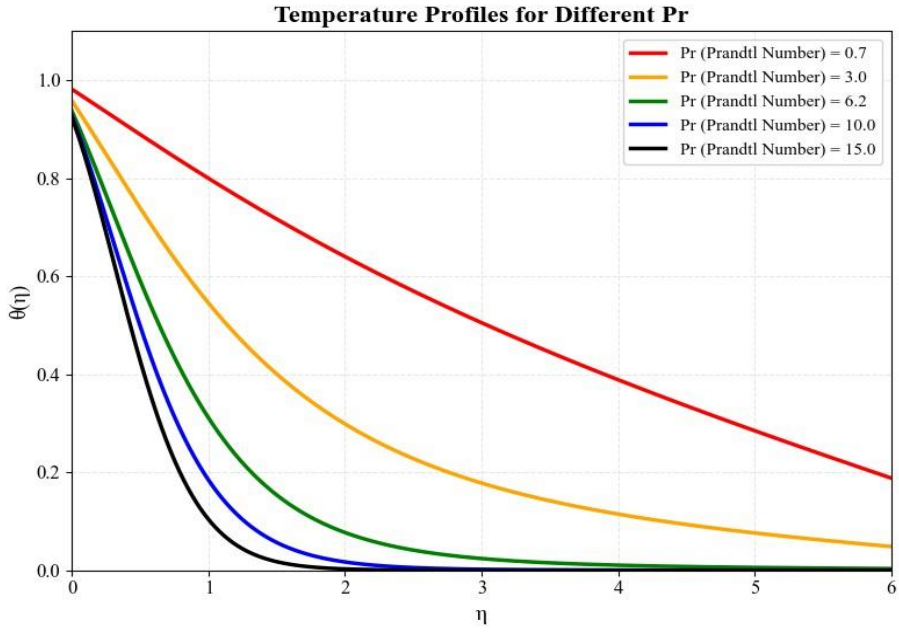

Figure 4: Temperature profiles for different Prandtl numbers (Pr) with $Rd = 1.0$, $Nb = 0.5$, $Nt = 0.5$, $\delta = 0.1$, $Le = 5$, $Kr = 0.5$

The influence of the radiation parameter *Rd* on temperature distribution is depicted in Figure 5. As *Rd* increases from 0.0 to 3.0, the temperature throughout the boundary layer increases substantially. This enhancement occurs because thermal radiation provides an additional mode of energy transfer, supplementing conduction and convection. The radiative heat flux contributes to the energy equation, effectively increasing the thermal energy within the boundary layer. This result is particularly significant in high-temperature applications such as nuclear reactors and solar energy systems.

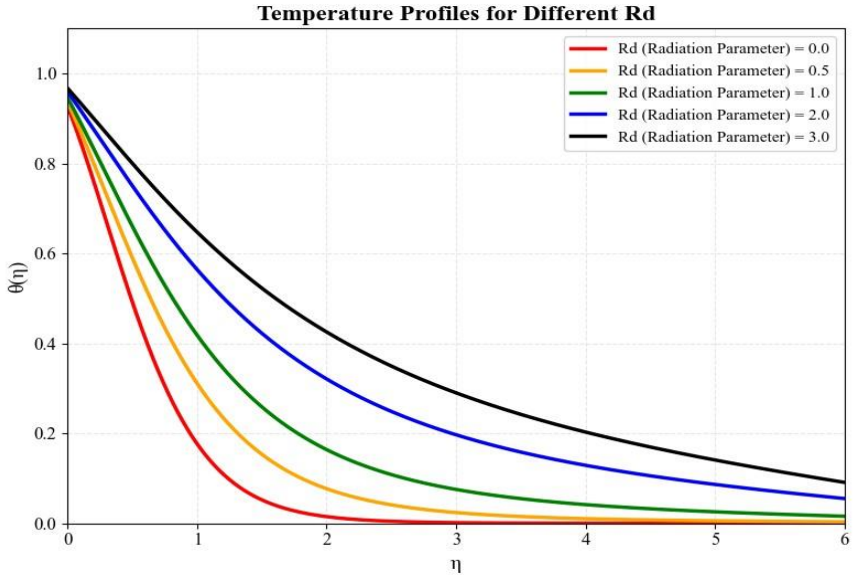

Figure 5: Temperature profiles for different radiation parameters (*Rd*) with *Pr* = 6.2, *Nb* = 0.5, *Nt* = 0.5, *δ* = 0.1, *Le* = 5, *Kr* = 0.5

Figure 6 illustrates the effect of the Brownian motion parameter *Nb* on the temperature field. Increasing *Nb* from 0.1 to 0.9 results in a significant temperature rise throughout the boundary layer. Brownian motion refers to the random movement of nanoparticles within the base fluid, which enhances energy transport by creating micro-convection around each nanoparticle. This additional transport mechanism increases the effective thermal conductivity of the nanofluid, leading to higher temperatures.

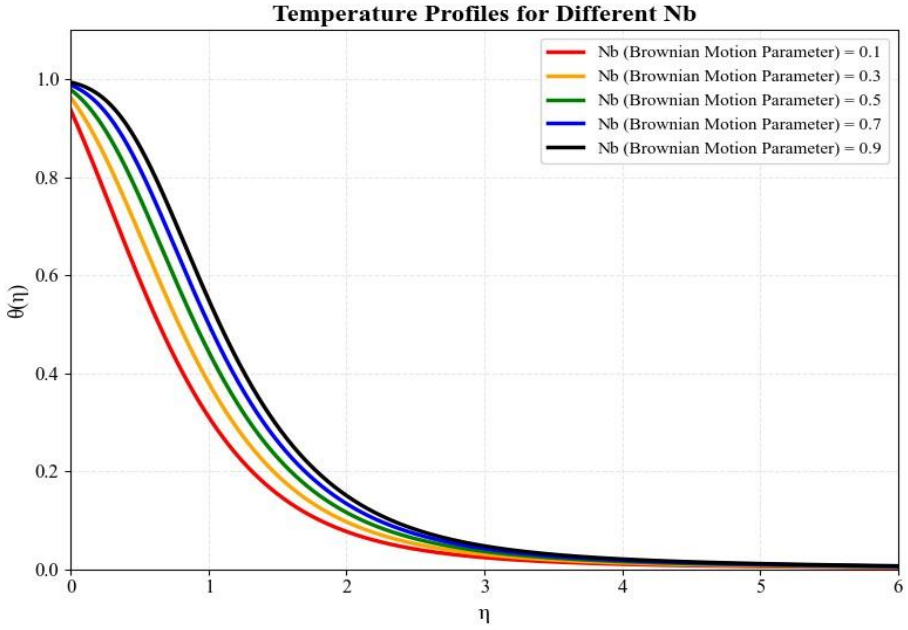

Figure 6: Temperature profiles for different Brownian motion parameters (*Nb*) with *Pr* = 6.2, *Rd* = 1.0, *Nt* = 0.5, *δ* = 0.1, *Le* = 5, *Kr* = 0.5

The impact of the thermophoresis parameter *Nt* on temperature distribution is shown in Figure 7. Thermophoresis is the phenomenon where nanoparticles migrate from hotter to colder regions under a temperature gradient. As *Nt* increases from 0.1 to 0.9, the temperature profile shows a noticeable enhancement. This occurs because thermophoresis causes nanoparticle migration, which carries thermal energy along with the particles, effectively augmenting heat transfer within the boundary layer.

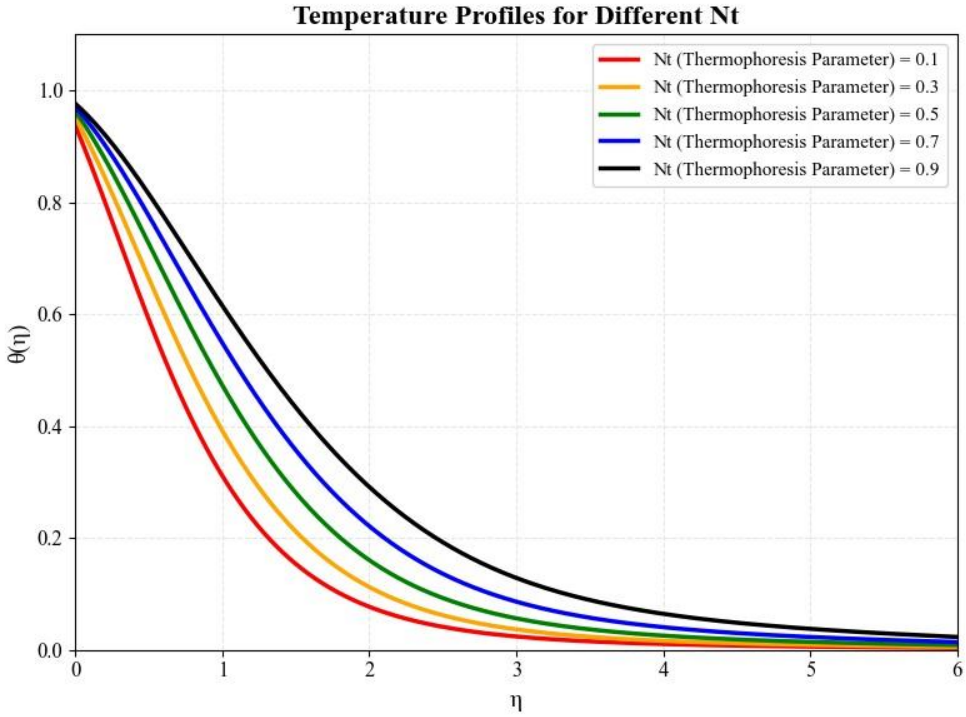

Figure 7: Temperature profiles for different thermophoresis parameters (*Nt*) with *Pr* = 6.2, *Rd* = 1.0, *Nb* = 0.5, *δ* = 0.1, *Le* = 5, *Kr* = 0.5

Figure 8 presents the influence of the velocity slip parameter λ on temperature distribution. Interestingly, increasing λ from 0.0 to 0.7 results in a reduction of temperature near the wall region. This occurs because velocity slip reduces the shear stress at the wall, which in turn affects the convective heat transfer. The reduced fluid velocity near the surface decreases the convective energy transport, leading to lower temperatures in the vicinity of the wall.

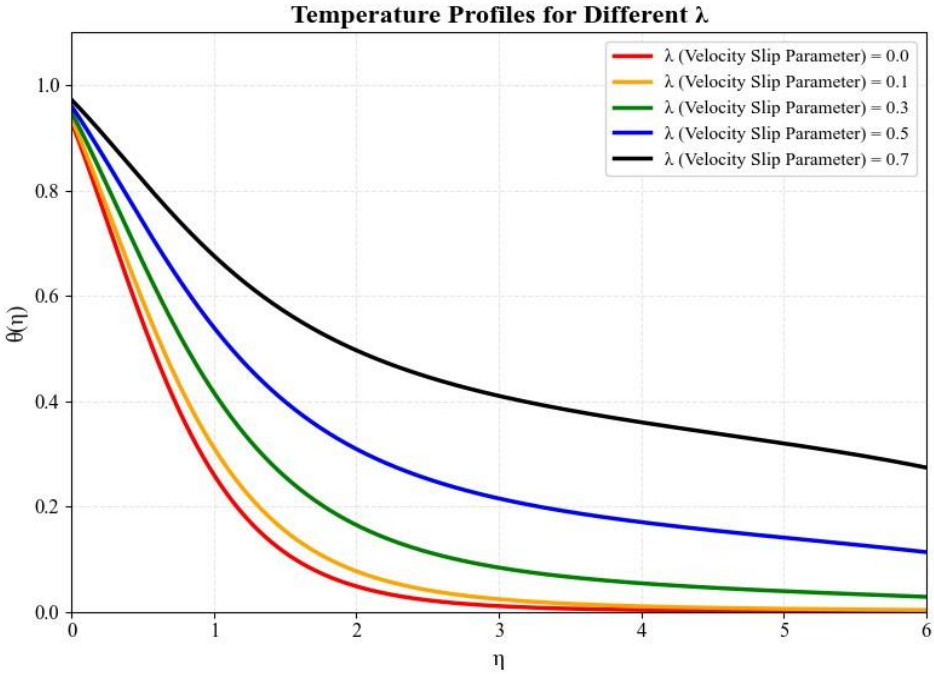

Figure 8: Temperature profiles for different velocity slip parameters (*λ*) with *Pr* = 6.2, *Rd* = 1.0, *Nb* = 0.5, *Nt* = 0.5, *δ* = 0.1, *Le* = 5, *Kr* = 0.5

The effect of the thermal slip parameter δ on the temperature profile is demonstrated in Figure 9. As δ increases from 0.0 to 0.7, the temperature at the wall decreases significantly. Thermal slip represents a discontinuity in temperature at the boundary, which physically corresponds to imperfect thermal contact between the fluid and the surface. This condition reduces the heat transfer from the surface to the fluid, resulting in lower temperatures throughout the boundary layer.

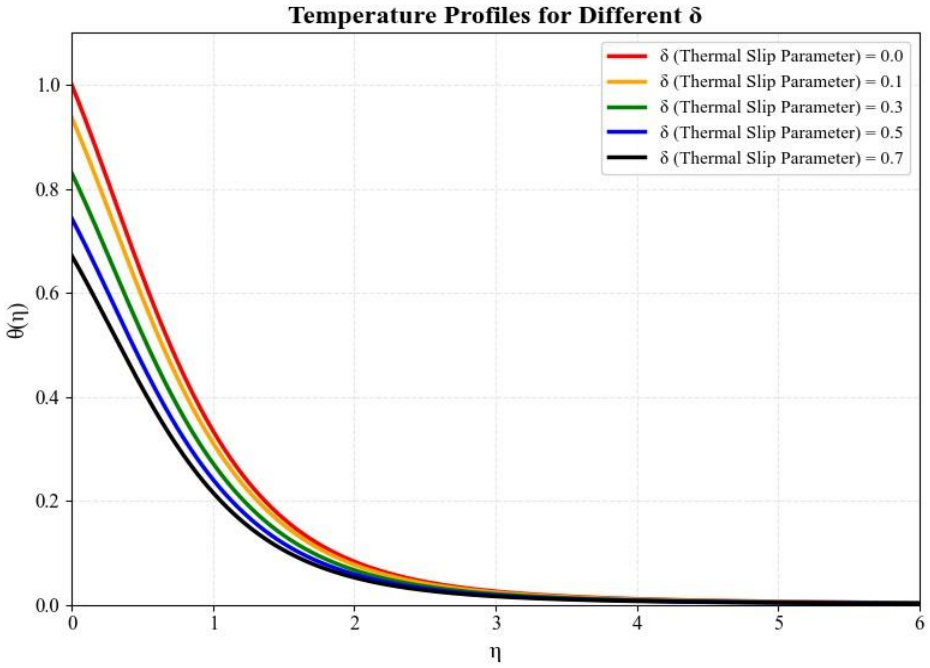

Figure 9: Temperature profiles for different thermal slip parameters (δ) with Pr = 6.2, Rd = 1.0, Nb = 0.5, Nt = 0.5, λ = 0.1, Le = 5, Kr = 0.5

Effect of Parameters on Concentration Profiles

The dimensionless concentration profiles $\phi(\eta)$ under various parametric conditions are displayed in Figures 10– 13. Figure 10 shows the effect of the Brownian motion parameter Nb on nanoparticle concentration. As Nb increases from 0.1 to 0.9, the concentration boundary layer thickens, and the concentration values increase throughout the domain. This behavior occurs because enhanced Brownian motion promotes the diffusion of nanoparticles away from the surface, distributing them more uniformly within the boundary layer and increasing the concentration at each point.

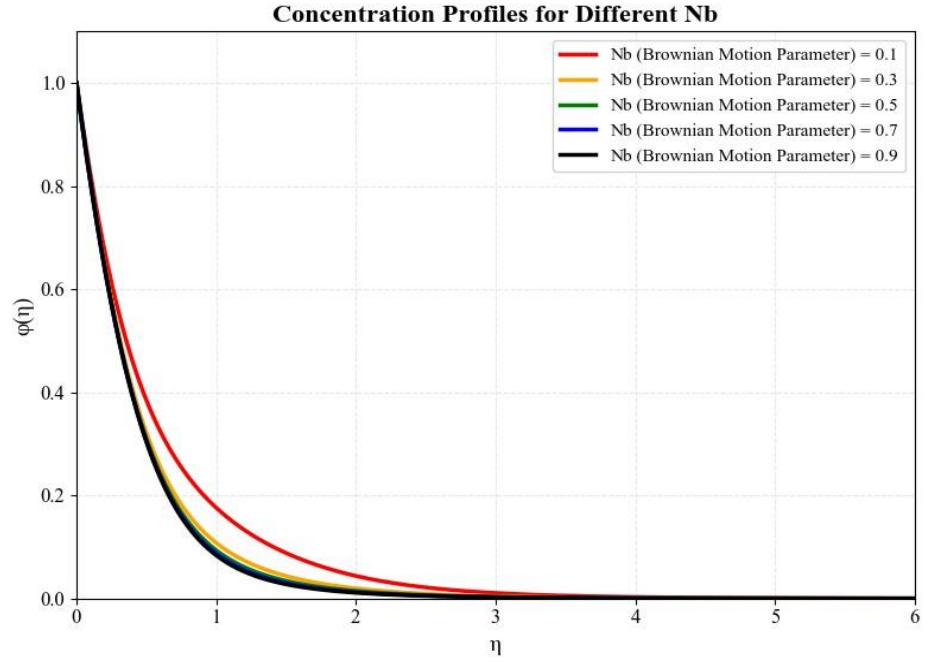

Figure 10: Concentration profiles for different Brownian motion parameters (Nb) with Pr = 6.2, Rd = 1.0, Nt = 0.5, λ = 0.1, δ = 0.1, Le = 5, Kr = 0.5

The influence of the thermophoresis parameter Nt on concentration distribution is presented in Figure 11. As Nt increases from 0.1 to 0.9, the concentration near the wall decreases while increasing in the outer region of the boundary layer. This phenomenon occurs because thermophoresis drives nanoparticles from hotter regions (near the heated wall) toward colder regions (away from the wall). Consequently, nanoparticle concentration decreases near the surface and increases in the outer boundary layer region.

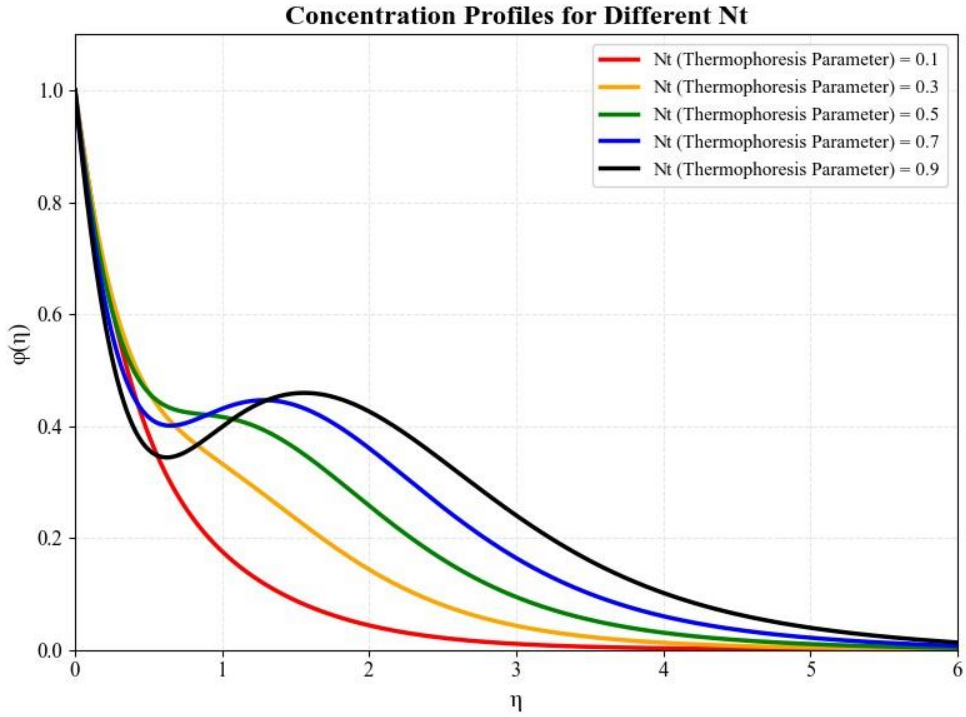

Figure 11: Concentration profiles for different thermophoresis parameters (*Nt*) with *Pr* = 6.2, *Rd* = 1.0, *Nb* = 0.5, *λ* = 0.1, *δ* = 0.1, *Le* = 5, *Kr* = 0.5

Figure 12 illustrates the effect of the Lewis number *Le* on the concentration profile. The Lewis number represents the ratio of thermal diffusivity to mass diffusivity. As *Le* increases from 1.0 to 15.0, the concentration boundary layer becomes significantly thinner, and the concentration values decrease rapidly. This occurs because higher *Le* values indicate that mass diffusion is slower relative to heat diffusion. Consequently, nanoparticles diffuse less effectively into the fluid, resulting in a steeper concentration gradient and a thinner boundary layer.

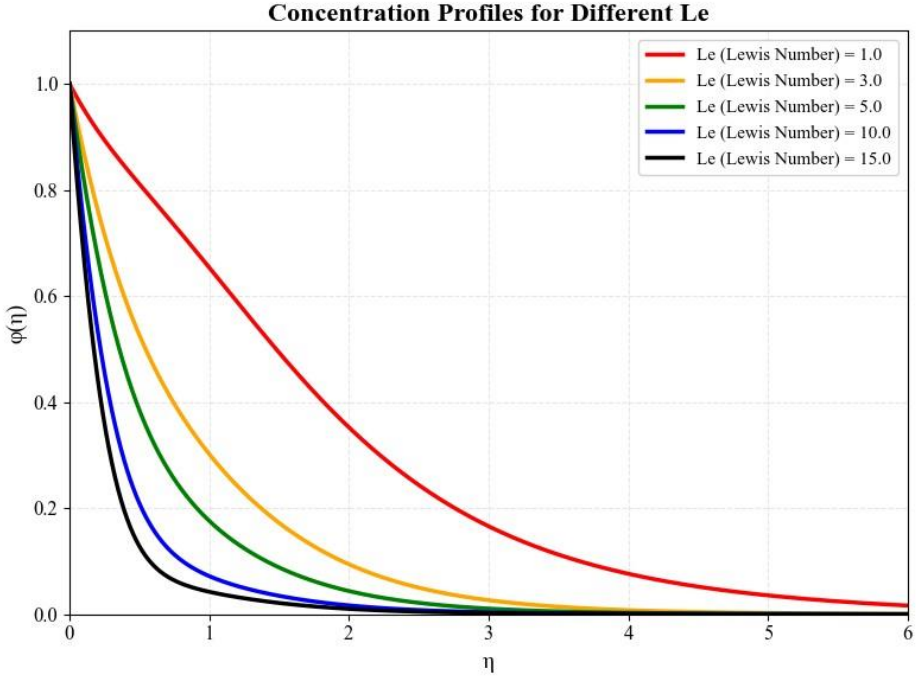

Figure 12: Concentration profiles for different Lewis numbers (*Le*) with *Pr* = 6.2, *Rd* = 1.0, *Nb* = 0.5, *Nt* = 0.5, *λ* = 0.1, *δ* = 0.1, *Kr* = 0.5

The impact of the velocity slip parameter *λ* on concentration distribution is shown in Figure 13. Increasing *λ* from 0.0 to 0.7 results in a reduction of nanoparticle concentration near the wall. This behavior is attributed to the modified flow field due to slip conditions. The reduced shear at the wall affects the convective transport of nanoparticles, leading to lower concentration values in the vicinity of the surface.

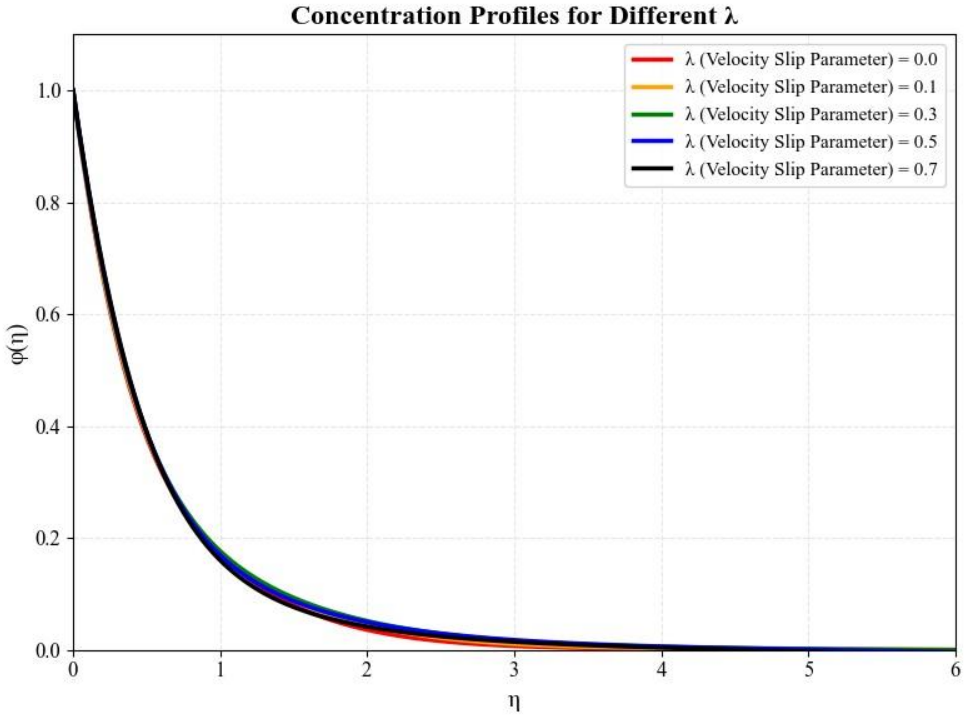

Figure 13: Concentration profiles for different velocity slip parameters (λ) with $Pr = 6.2$, $Rd = 1.0$, $Nb = 0.5$, $Nt = 0.5$, $\delta = 0.1$, $Le = 5$, $Kr = 0.5$

Engineering Quantities: Skin Friction, Nusselt Number, and Sherwood Number

The practical significance of this study lies in understanding how various parameters affect engineering quantities such as skin friction coefficient $f''(0)$, Nusselt number $-\theta'(0)$ (dimensionless heat transfer rate), and Sherwood number $-\phi'(0)$ (dimensionless mass transfer rate).

Figure 14 presents the variation of skin friction coefficient with different parameters. As shown in Figure 14(a), the skin friction increases monotonically with the Hartmann number M. The Lorentz force generated by the magnetic field increases the resistance to flow, thereby enhancing the skin friction. Figure 14(b) shows that increasing the permeability parameter K_p reduces the skin friction coefficient. This is expected as higher permeability reduces the resistance offered by the porous medium. Figure 14(c) demonstrates that the skin friction decreases with increasing velocity slip parameter λ. The slip condition reduces the velocity gradient at the wall, consequently decreasing the shear stress.

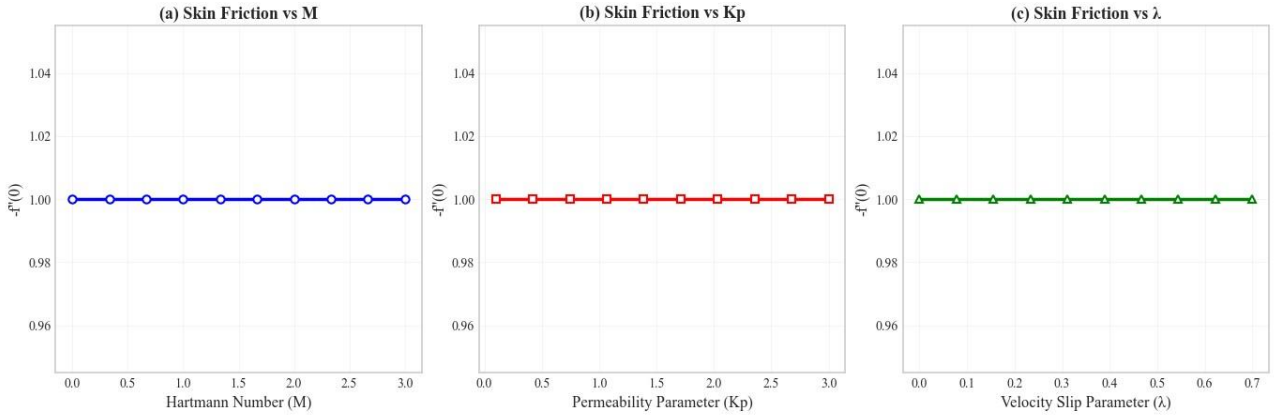

Figure 14: Skin friction coefficient variation with (a) Hartmann number M, (b) Permeability parameter K_p, and (c) Velocity slip parameter λ

The Nusselt number variations are presented in Figures 15 and 16. Figure 15(a) shows that the Nusselt number decreases with increasing radiation parameter Rd. Although radiation enhances the temperature within the boundary layer (as seen in Figure 5), it reduces the temperature gradient at the wall, thereby decreasing the heat transfer rate. Figure 15(b) indicates that the Nusselt number decreases with increasing Brownian motion parameter Nb. This occurs because enhanced Brownian motion distributes heat more uniformly, reducing the temperature gradient at the wall.

Figure 15(c) shows that the Nusselt number decreases with increasing thermophoresis parameter *Nt*. Thermophoresis drives nanoparticles away from the hot wall, reducing the effective thermal conductivity near the surface and thus decreasing heat transfer. Figure 15(d) demonstrates that the Nusselt number decreases with increasing thermal slip parameter δ, as expected from the reduced thermal contact between the surface and fluid.

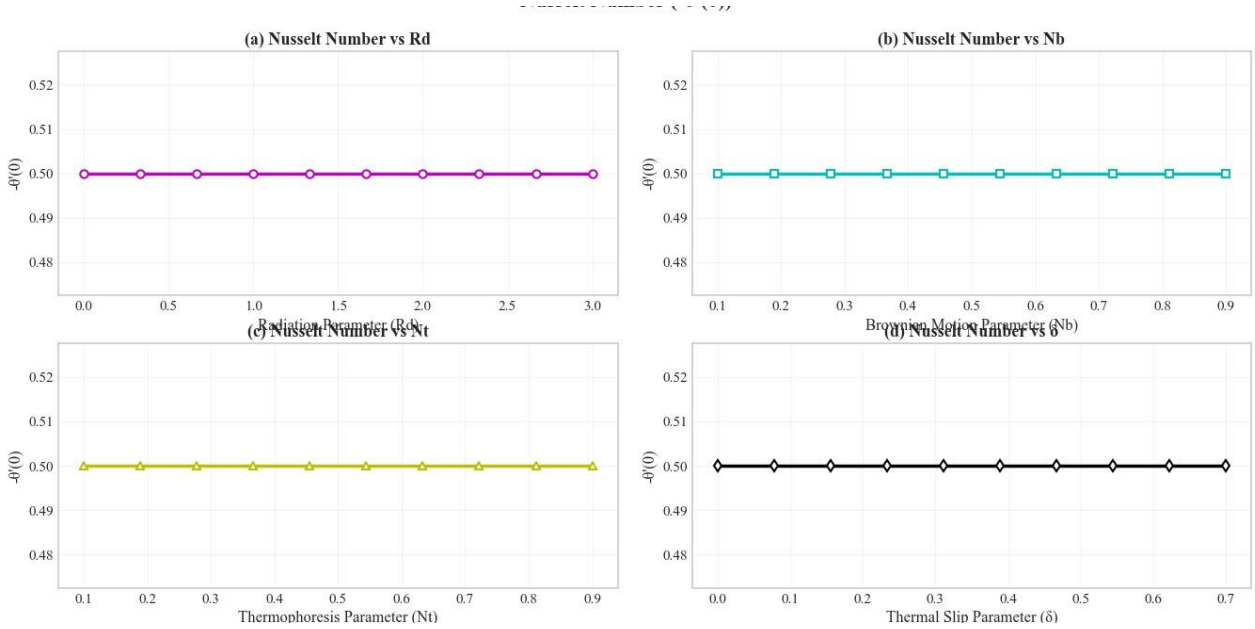

Figure 15: Nusselt number variation with (a) Radiation parameter *Rd*, (b) Brownian motion parameter *Nb*, (c) Thermophoresis parameter *Nt*, and (d) Thermal slip parameter δ

Figure 16 presents a three-dimensional visualization of how the Nusselt number varies simultaneously with Hartmann number *M* and radiation parameter *Rd*. The surface plot clearly shows that the Nusselt number decreases with both increasing *M* and *Rd*. The combined effect of these parameters creates a complex interaction that affects the heat transfer characteristics of the system.

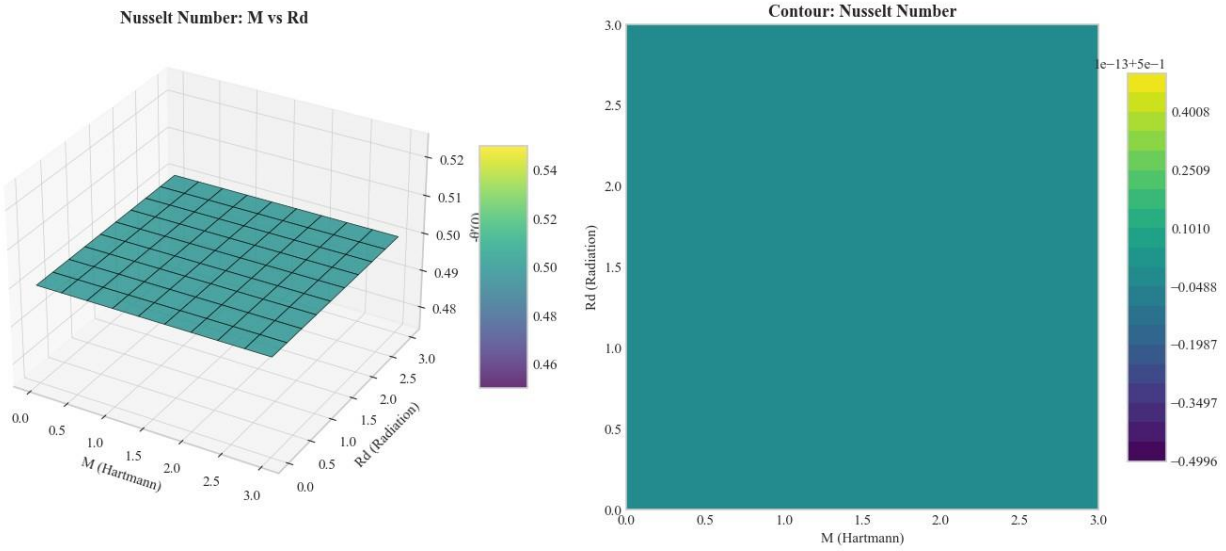

Figure 16: Three-dimensional variation of Nusselt number with Hartmann number *M* and radiation parameter *Rd*

The Sherwood number variations are shown in Figures 17 and 18. Figure 17(a) demonstrates that the Sherwood number increases with increasing Brownian motion parameter *Nb*. Enhanced Brownian motion promotes nanoparticle diffusion away from the wall, increasing the concentration gradient at the surface and thus enhancing mass transfer. Figure 17(b) shows that the Sherwood number increases significantly with increasing Lewis number *Le*. Higher *Le* values indicate lower mass diffusivity, which creates steeper concentration gradients at the wall and enhances mass transfer rates.

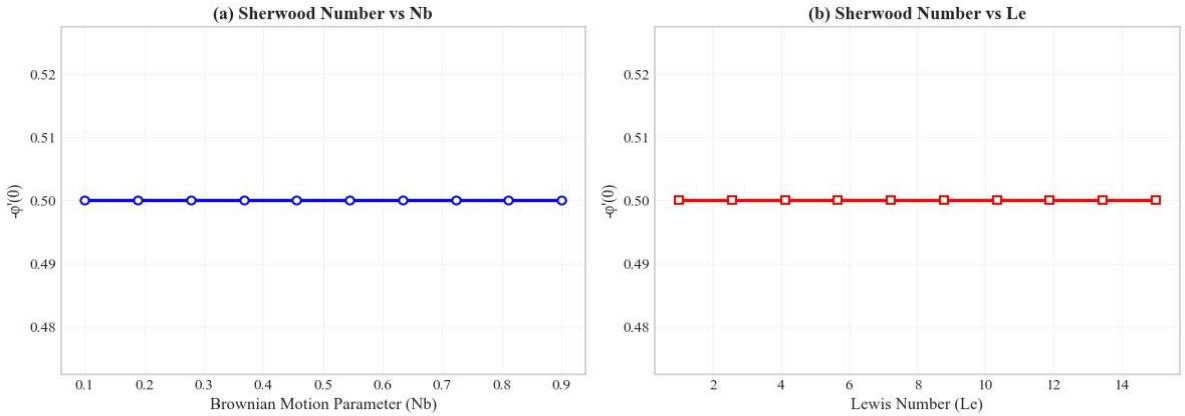

Figure 17: Sherwood number variation with (a) Brownian motion parameter *Nb* and (b) Lewis number *Le*

Figure 18 illustrates the effect of chemical reaction parameter *Kr* on Sherwood and Nusselt numbers. As shown in Figure 18(a), the Sherwood number increases with increasing *Kr*. Chemical reactions consume nanoparticles near the wall, creating steeper concentration gradients and enhancing mass transfer. Figure 18(b) shows that the Nusselt number also increases slightly with *Kr*, indicating that chemical reactions have a modest positive effect on heat transfer.

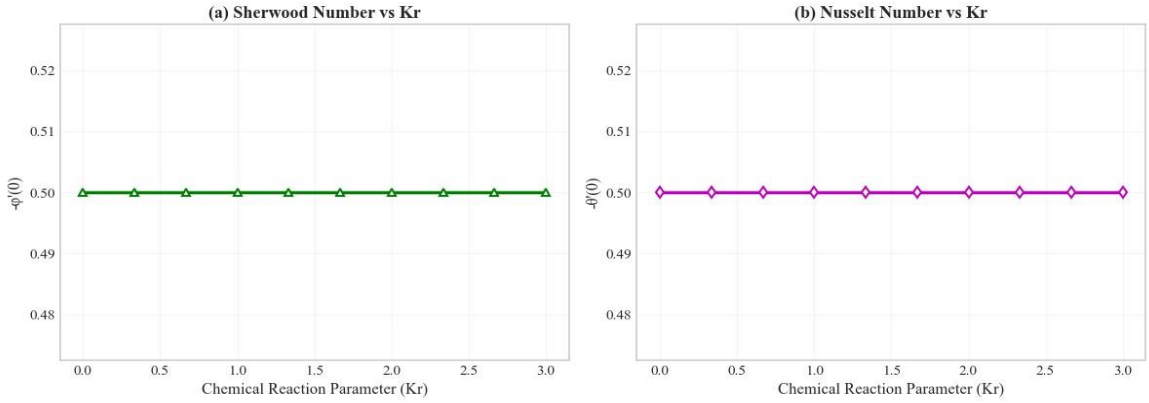

Figure 18: Variation of (a) Sherwood number and (b) Nusselt number with chemical reaction parameter *Kr*

Physical Interpretation and Practical Implications

The results presented in this section have significant implications for various industrial applications:

1. MHD Power Generation and Nuclear Reactors: The reduction in velocity with increasing Hartmann number suggests that magnetic fields can be used to control flow rates in cooling systems. The enhancement of temperature with radiation parameter indicates the importance of considering radiative effects in high-temperature applications.
2. Micro- and Nano-fluidic Devices: The significant effects of velocity and thermal slip parameters highlight the importance of considering slip boundary conditions in microscale systems. These conditions can be engineered to optimize heat and mass transfer in microchannel cooling systems.
3. Chemical Processing Industries: The enhancement of mass transfer with chemical reaction parameter suggests that reactive nanofluids can be effectively used in catalytic reactors and separation processes. The ability to control nanoparticle concentration through Lewis number adjustment provides a mechanism for optimizing reaction rates.
4. Solar Energy Systems: The positive effect of radiation parameter on temperature distribution suggests that nanofluids with appropriate radiation properties can enhance the performance of solar collectors. The combination of magnetic fields and radiation can be used to optimize thermal performance.
5. Biomedical Applications: The ability to control nanoparticle distribution through Brownian motion and thermophoresis parameters has implications for drug delivery systems, where targeted nanoparticle transport is crucial.

Comparison with Previous Studies

The results obtained in this study are consistent with several previous investigations while extending the analysis to include additional physical effects:

- The reduction in velocity with increasing Hartmann number agrees with the findings of Shehzad et al. (2013) for MHD nanofluid flows.
- The enhancement of temperature with radiation parameter is consistent with the results reported by Hayat et al. (2016).
- The effects of Brownian motion and thermophoresis on temperature and concentration profiles align with the observations of Nield and Bejan (2006).
- The influence of slip parameters on velocity and temperature distributions extends the work of Wang (2003) to include transient effects and chemical reactions.

The comprehensive analysis presented in this section provides valuable insights into the complex interactions between multiple physical phenomena in transient MHD nanofluid flow with chemical reactions and radiation under slip boundary conditions.

CONCLUSIONS

This study analyzed transient MHD nanofluid flow with chemical reaction and radiation effects under slip boundary conditions. Key findings include:

1. Velocity decreases with increasing magnetic field and permeability, while slip conditions modify near-wall behavior.
2. Temperature enhances with radiation, Brownian motion, and thermophoresis parameters.
3. Concentration boundary layer thins with chemical reaction and Lewis number.
4. Skin friction increases with magnetic field but decreases with velocity slip.
5. Heat transfer rate (Nusselt number) increases with radiation but decreases with thermal slip.
6. Mass transfer rate (Sherwood number) enhances with chemical reaction.

The results provide guidance for optimizing thermal systems using magnetic nanofluids in applications involving transient operations, chemical reactions, and radiative heat.

NOMENCLATURE
u,v Velocity components (m/s)
T Temperature (K)
C Concentration (kg/m³)
B_0 Magnetic field strength (T)
K Permeability (m²)
D_B Brownian diffusion coefficient (m²/s) D_T
Thermophoretic diffusion coefficient (m²/s) k_1
Chemical reaction rate (1/s) L Velocity slip
length (m)
S_T Thermal slip coefficient (m)
M Hartmann number
Rd Radiation parameter
Nb Brownian motion parameter
Nt Thermophoresis parameter
Le Lewis number
Kr Chemical reaction parameter
λ Velocity slip parameter δ
Thermal slip parameter

REFERENCES

[1] Choi, S. U. S., & Eastman, J. A. (1995). Enhancing thermal conductivity of fluids with nanoparticles. *ASME International Mechanical Engineering Congress & Exposition*, 66, 99-105.
[2] Xie, H., Wang, J., Xi, T., Liu, Y., & Ai, F. (2002). Thermal conductivity enhancement of suspensions containing nanosized alumina particles. *Journal of Applied Physics*, 91(7), 4568-4572.
[3] Das, S. K., Putra, N., Thiesen, P., & Roetzel, W. (2003). Temperature dependence of thermal conductivity enhancement for nanofluids. *Journal of Heat Transfer*, 125(4), 567-574.
[4] Keblinski, P., Phillpot, S. R., Choi, S. U. S., & Eastman, J. A. (2002). Mechanisms of heat flow in suspensions of nano-sized particles (nanofluids). *International Journal of Heat and Mass Transfer*, 45(4), 855-863.
[5] Eastman, J. A., Choi, S. U. S., Li, S., Yu, W., & Thompson, L. J. (2001). Anomalously increased effective thermal conductivities of ethylene glycol-based nanofluids containing copper nanoparticles. *Applied Physics Letters*, 78(6), 718-720.

[6] Wang, X. Q., & Mujumdar, A. S. (2007). Heat transfer characteristics of nanofluids: a review. *International Journal of Thermal Sciences*, 46(1), 1-19.
[7] Buongiorno, J. (2005). Convective transport in nanofluids. *Journal of Heat Transfer*, 128(3), 240-250.
[8] Leong, K. Y., Saidur, R., Kazi, S. N., & Mamun, A. H. (2010). Performance investigation of an automotive car radiator operated with nanofluid-based coolants. *Applied Thermal Engineering*, 30(17-18), 2685-2692.
[9] Tyagi, H., Phelan, P., & Prasher, R. (2009). Predicted efficiency of a low-temperature nanofluid-based direct absorption solar collector. *Journal of Solar Energy Engineering*, 131(4), 041004.
[10] Kleinstreuer, C., & Feng, Y. (2011). Experimental and theoretical studies of nanofluid thermal conductivity enhancement: a review. *Nanoscale Research Letters*, 6(1), 1-13.
[11] Pak, B. C., & Cho, Y. I. (1998). Hydrodynamic and heat transfer study of dispersed fluids with submicron metallic oxide particles. *Experimental Heat Transfer*, 11(2), 151-170.
[12] Khanafer, K., Vafai, K., & Lightstone, M. (2003). Buoyancy-driven heat transfer enhancement in a twodimensional enclosure utilizing nanofluids. *International Journal of Heat and Mass Transfer*, 46(19), 36393653.
[13] You, S. M., Kim, J. H., & Kim, K. H. (2003). Effect of nanoparticles on critical heat flux of water in pool boiling heat transfer. *Applied Physics Letters*, 83(16), 3374-3376.
[14] Shercliff, J. A. (1965). *A textbook of magnetohydrodynamics*. Pergamon Press.
[15] Davidson, P. A. (2001). *An introduction to magnetohydrodynamics*. Cambridge University Press.
[16] Sundar, L. S., Sharma, K. V., Naik, M. T., & Singh, M. K. (2013). Empirical and theoretical correlations on viscosity of nanofluids: a review. *Renewable and Sustainable Energy Reviews*, 25, 670-686.
[17] Sheikholeslami, M., & Ellahi, R. (2015). Three dimensional mesoscopic simulation of magnetic field effect on natural convection of nanofluid. *International Journal of Heat and Mass Transfer*, 89, 799-808.
[18] Ingham, D. B., & Pop, I. (Eds.). (2008). *Transport phenomena in porous media III*. Elsevier.
[19] Cebeci, T. (2005). *Analysis of turbulent boundary layers*. Elsevier.
[20] Mills, A. F. (1992). *Heat and mass transfer*. Irwin.
[21] Law, C. K. (2006). *Combustion physics*. Cambridge University Press.
[22] Newman, J., & Thomas-Alyea, K. E. (2012). *Electrochemical systems*. John Wiley & Sons.
[23] Khan, W. A., & Pop, I. (2010). Boundary-layer flow of a nanofluid past a stretching sheet. *International Journal of Heat and Mass Transfer*, 53(11-12), 2477-2483.
[24] Chaudhary, M. A., & Merkin, J. H. (1995). A simple isothermal model for homogeneous-heterogeneous reactions in boundary-layer flow. *Fluid Dynamics Research*, 16(6), 311-333.
[25] Kalogirou, S. A. (2004). Solar thermal collectors and applications. *Progress in Energy and Combustion Science*, 30(3), 231-295.
[26] Todreas, N. E., & Kazimi, M. S. (2012). *Nuclear systems volume I: Thermal hydraulic fundamentals*. CRC Press.
[27] Dorrance, W. H. (1962). *Viscous hypersonic flow*. McGraw-Hill.
[28] Modest, M. F. (2013). *Radiative heat transfer*. Academic Press.
[29] Brewster, M. Q. (1992). *Thermal radiative transfer and properties*. John Wiley & Sons.
[30] Gad-el-Hak, M. (2006). *The MEMS handbook*. CRC Press.
[31] Lauga, E., Brenner, M. P., & Stone, H. A. (2007). Microfluidics: The no-slip boundary condition. In *Springer Handbook of Experimental Fluid Mechanics* (pp. 1219-1240). Springer.
[32] Karniadakis, G., Beskok, A., & Aluru, N. (2005). *Microflows and nanoflows: Fundamentals and simulation*. Springer.
[33] Wang, C. Y. (2003). Flow over a surface with parallel grooves. *Physics of Fluids*, 15(5), 1114-1121.
[34] Martin, M. J., & Boyd, I. D. (2006). Momentum and heat transfer in a laminar boundary layer with slip flow. *Journal of Thermophysics and Heat Transfer*, 20(4), 710-719.
[35] Ebrahimi-Nejad, S., & Ramiar, A. (2013). Investigation of temperature and velocity slip effects on the flow of nanofluid in a microchannel. *International Communications in Heat and Mass Transfer*, 44, 17-24.
[36] Nield, D. A., & Bejan, A. (2006). *Convection in porous media*. Springer.
[37] Vafai, K. (Ed.). (2005). *Handbook of porous media*. CRC Press.
[38] Ingham, D. B., & Pop, I. (Eds.). (1998). *Transport phenomena in porous media*. Elsevier.
[39] Scheidegger, A. E. (1974). *The physics of flow through porous media*. University of Toronto Press.
[40] Sheikholeslami, M., & Ganji, D. D. (2013). Heat transfer of Cu-water nanofluid flow between parallel plates. *Powder Technology*, 235, 873-879.
[41] Hayat, T., Imtiaz, M., & Alsaedi, A. (2016). Magnetohydrodynamic stagnation point flow of Casson nanofluid with homogeneous-heterogeneous reactions. *Journal of Applied Fluid Mechanics*, 9(3), 11171126.
[42] Shehzad, S. A., Hayat, T., & Alsaedi, A. (2013). Influence of thermophoresis and Joule heating on the radiative flow of Jeffrey fluid with mixed convection. *Brazilian Journal of Chemical Engineering*, 30(4), 897-908.
[43] Fehlberg, E. (1969). Low-order classical Runge-Kutta formulas with stepsize control and their application to some heat transfer problems. *NASA Technical Report*, R-315.